CrossMark

Synthesis and characterization of Ni^{2+} ions incorporated CuO nanoparticles and its application in antibacterial activity

S. Ramya[1] · G. Viruthagiri[1] · R. Gobi[1] · N. Shanmugam[1] · N. Kannadasan[2]

Abstract In this present work, Ni doped CuO nanoparticles were successfully prepared by chemical precipitation method. The structural and chemical compositions of the products were characterized by X-ray diffraction, Fourier transform infrared spectroscopy and X-ray photoelectron spectroscopy. The obtained products were identified to be of monoclinic structure and these results demonstrate that the Ni ions were substituted into the CuO lattice. The optical properties of the products were studied by diffuse reflectance spectroscopy and room temperature photoluminescence measurements. The morphological analyses were obtained by using field emission scanning electron microscopy and transmission electron microscopy. The magnetic properties were investigated at room temperature using the vibrating sample magnetometer and the hysteresis loops confirmed the ferromagnetic behaviour of CuO on doping due to smaller size effect. Further, as-formed doped and undoped CuO nanoparticles exhibit significant antibacterial activity against pathogenic bacterial strains namely Gram −ve (*Pseudomonas aeruginosa*, and *Escherichia coli*), Gram +ve bacteria (*Bacillus subtilis*, *Staphylococcus aureus*).

✉ G. Viruthagiri
  gvgiri2002@gmail.com

  R. Gobi
  alankoffi007@yahoo.co.in

[1] Department of Physics, Annamalai University, Annamalai Nagar, Chidambaram, Tamilnadu 608 002, India

[2] Department of Physics, BWDA Arts and Science College, Kolliyangunam, Mailam, Tamilnadu 604 304, India

1 Introduction

Transition metal nanoparticles are the frontrunners in material research because of its unique physical and chemical properties that largely differ from those of their bulk materials which facilitate them in device based applications. Among transition metal nanoparticles, copper oxide (CuO), is an important p-type metal oxide with a narrow band gap (1.4 eV), has received significant attention in past decades in spintronic devices because its Curie temperature is theoretically predicted to be well above the room temperature [1], low cost, non-toxicity, ease of production, high specific capacitances, and ease of storage [2]. In general, metal doping makes radical changes in optical, electrical, and magnetic properties of CuO by altering its electronic structure. Also, Cu has three oxidation states, Cu^{+}, Cu^{2+} and Cu^{3+} therefore both hole doping and electron doping mechanisms are possible [1].

There are many literatures reported on the changes associated, when CuO is doped with transition metals, such as Ni [3], Mn [4, 5], Fe [6, 7], Fe and Ni co-doped [8] Ti, Cd and Zn [9]. While, Ni doped CuO nanoparticles may give the new information about the structural, optical and magnetic properties. In the present trend, microbes are playing an important role in the propagation of commuable diseases. Therefore, knowledge on the microbes and their control are essential need of their moment. Usually metal oxide nanoparticles like CuO can play a role of antimicrobial agent since it has high resistance to the strains. The bacterial property of such materials majorly depends on their size, stability and concentration [10].

Various physical and chemical methods have been developed for obtaining the CuO nanoparticles: such as sol–gel [11] chemical method [12], hydrothermal method [13], electrochemical method [14], combustion synthesis

🖉 Springer

[9], co-precipitation [15], sonochemical synthesis [16], etc. Among the different methods, the chemical precipitation method has many advantages over other synthesis methods because of its simple, inexpensive and versatile method for preparing the metallic nanoparticles.

The aim of the present study is to investigate the structure, morphology, optical and magnetic properties of Ni doped CuO nanostructures by chemical precipitation method with varying Ni-content of 0.05, 0.075, 0.1 and 0.125 M. The obtained powders were characterized using powder X-ray diffraction (XRD) analysis, Fourier transform infrared (FTIR) spectroscopy and X-ray photoelectron spectroscopy (XPS), Field emission scanning electron microscopy (FE-SEM), high resolution transmission electron microscopy (HR-TEM). Energy dispersive X-ray analyses (EDX), UV–Vis diffuse reflectance spectroscopy (UV–Vis–DRS), and photoluminescence (PL) spectroscopy. In addition magnetic measurements were carried out using vibrating sample magnetometer (VSM) at room temperature.

2 Materials and methods

2.1 Reagents

Copper acetate ($C_4H_6CuO_4 \cdot 4H_2O$), Nickel (II) nitrate (Ni $(NO_3)_2 \cdot 6H_2O$), potassium hydroxide (KOH), absolute ethanol, acetone were of analytical reagent (AR) grade, purchased from Merck (assay ≥ 99 %) and used without further purification. Also, double distilled water was used throughout all experiments.

2.2 Synthesis of pure and Ni doped CuO nanoparticles

Pure and Ni-doped (0.05, 0.075, 0.1 and 0.125 M) CuO nanoparticles were synthesized by a simple chemical precipitation method. 0.5 M of copper acetate ($C_4H_6CuO_4 \cdot 4H_2O$) was dissolved in 50 ml of distilled water and stirred for 15 min. Then, 1.5 M of potassium hydroxide (KOH) was dissolved in 50 ml of distilled water and the solution was added drop wise into the above solution under constant stirring. The obtained blue precipitate of copper hydroxide was stirred and heated at 60 °C until a black precipitate was formed. The resultant precipitate was filtered and washed with distilled water and absolute ethanol in several times to remove the impurities. Finally, the product was dried in a hot air oven at 100 °C for 7 h to obtain pure CuO nanopowder. Ni (0.05, 0.075, 0.1, and 0.125 M) doping was achieved by adding appropriate amount of Nickel (II) nitrate (Ni $(NO_3)_2 \cdot 6H_2O$) to the initial solution. These samples were finally calcinated at 400 °C for 3 h in a muffle furnace.

2.3 Characterization

The synthesized pure and Ni doped CuO nanoparticles were characterized by different techniques. The powder XRD patterns were recorded on an X-ray diffractometer (X'PERTPRO) with monochromated CuKα radiation ($\lambda = 1.5406$ Å). The XPS spectra were recorded on an HP.5950A Hewlett-Packard spectrometer using an AlKα (hν = 1486.6 eV) X-ray excitation source. The FT-IR spectra were recorded with a FT-IR spectrometer (SHIMADZU-8400) with KBr pellets in the range of 4000–400 cm^{-1}. The UV–Vis absorption spectra of the samples were recorded on an UV–Vis–NIR spectrometer (Varian/carry-5000) with a wavelength range of 200–800 nm. The PL emission studies of the samples were carried out at a room temperature using Jobin–YVON, FLUOROLOG-FL3-11 spectroflurometer. The morphology and size distribution were characterized using FE–SEM (SUPRA 55) and HR-TEM measurement in a JEM–2100 instrument. Magnetic measurements were carried out at room temperature using a PMC Micro Mag 3900 model VSM equipped with 1 T magnet.

2.4 Antibacterial activity

Antibacterial activity was screened against four bacterial strains namely Gram −ve *Pseudomonas aeruginosa*, and *Escherichia coli,* Gram +ve bacteria *Bacillus subtilis* and *Staphylococcus aureus* by agar well diffusion method [17]. Nutrient Agar plates were prepared and swabbed using Sterile L-shaped glass rod with 100 μl of 24 h mature broth culture of individual bacterial strains. The wells were made by using sterile cork borer (6 mm) wells was created into the each Petri plates. Varied concentrations of Ni doped CuO Nps were used to assess the activity of the nanoparticles. The compounds were dispersed in sterile water and it was used as a negative control and simultaneously the standard antibiotics Gentamycin (10 μg/50 μl) (Hi Media, Mumbai, India) as positive control were tested against the bacterial pathogens. Then the plates were incubated at 37 °C for 24–36 h, the zone inhibition measured in millimeter (mm) of the every well and also the values were noted. Triplicates were maintained in every concentration and also the average values were calculated for the ultimate antibacterial activity.

3 Results and discussion

3.1 Structural analysis

The structural properties of prepared nanoparticles were investigated by XRD analysis. Figure 1 shows the XRD

patterns of pure and Ni (0.05–0.125 M) doped CuO nanoparticles. It revealed that the prepared nanoparticles are crystalline in nature with monoclinic CuO phase (space group C2/c). All the diffraction patterns corresponding to the planes such as (−110), (111), (002), (−202), (020), (202), (113), (−311), (−113), (311) and (004) are well matched with standard JCPDS (45-0937) of CuO. The dual prominent peaks of (002) and (111) lattice planes are observed in both pure and Ni doped concentrations.

The diffraction results show no impurity or secondary phase peaks up to 0.1 M of Ni-doping. However, when the concentration of doping was increased to 0.125 M, a secondary peak corresponding to CuO was predicted. This specifies that 0.1 M could be the dispersion limit of Ni^{2+} in the CuO matrix. The lattice parameters of the doped products do not show major variations since the ionic radius of Ni^{2+} (0.69 Å) is closer to the value of Cu^{2+} (0.73 Å). Using XRD analysis, the crystallite size of CuO particles is determined from the Debye–Scherrer's relation [18],
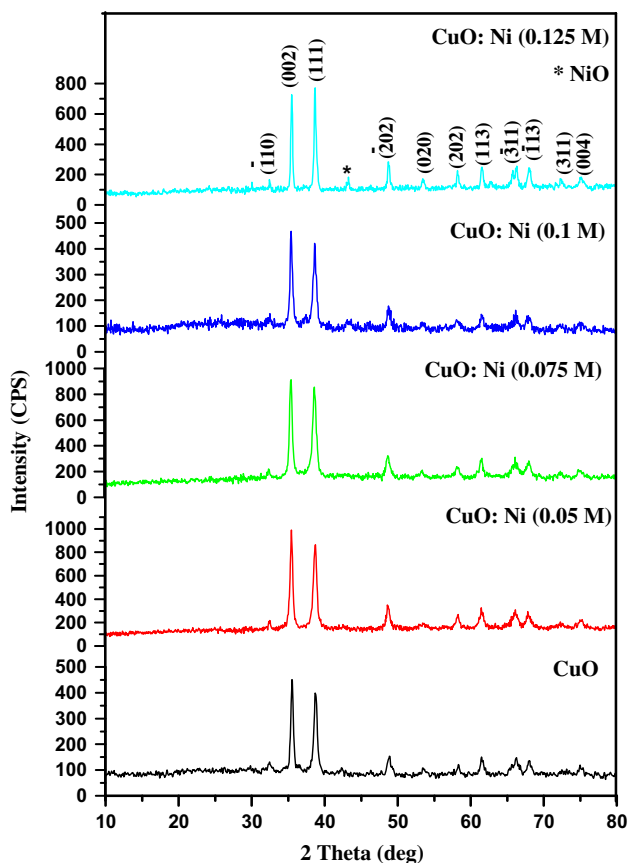
$$D = \frac{K\lambda}{\beta \cos\theta} \tag{1}$$

where K is the Scherrer constant, λ is the wavelength of light used for the diffraction, β is the full width at half maximum of the peaks and θ is the angle measured. The Scherrer constant (K) in the equation accounts for the shape of the particle and generally taken to have the value 0.9. Table 1 shows the calculated lattice parameters and the size of the crystallites are found to be in the range between 21.41 and 25.43 nm for pure and Ni doped CuO. The XRD patterns clearly depicted that the peak sharpening increased with the Ni content. From the structural studies, we have concluded that no other dramatic changes in CuO structure and nickel peak only occurred in the XRD patterns of CuO particles. These XRD patterns established that the nickel content played an important role in the structural properties of CuO nanoparticles.

3.2 X-ray photoelectron spectroscopy

The XPS technique is used to evaluate the valence state of doping element in Ni doped CuO nanoparticles along with their corresponding binding energies. Figure 2 depicts the overall XPS spectrum of Ni doped (0.1 M) CuO nanoparticles. The XPS spectrum of Cu 2p core level peaks is shown in Fig. 2b. The main two peaks are located at 934.3 and 954.2 eV which confirm the presence of Cu $2p_{3/2}$ and Cu $2p_{1/2}$ peaks, respectively [19]. In addition, the satellite peaks located at 943.3 and 962.9 eV specify the partially filled d-block ($3d_9$) of Cu^{2+} [20]. In Fig. 2c, Ni 2p spectrum exhibits two peaks at 855.3 and 873.5 eV, which are good agreement with the binding energies of Ni $2p_{3/2}$ and Ni $2p_{1/2}$ respectively. This indicates that the Ni ion in our samples is Ni 2p. Besides, the peaks located at 861.5 and 881.2 eV are satellite peaks of Ni 2p, which also proves the existence of Ni 2p [21] assigned to the Ni^{2+} (Ni–O bonds) in the NiO particles. Figure 2d shows two O 1s peaks of binding energies at around 530.3 and 531.8 eV could be assigned to O^{2-} (adsorbed oxygen) in CuO [22].

Fig. 1 X-ray diffraction patterns of CuO and various concentrations of Ni-doped CuO nanoparticles

Table 1 XRD derived parameters of undoped and Ni doped CuO nanoparticles

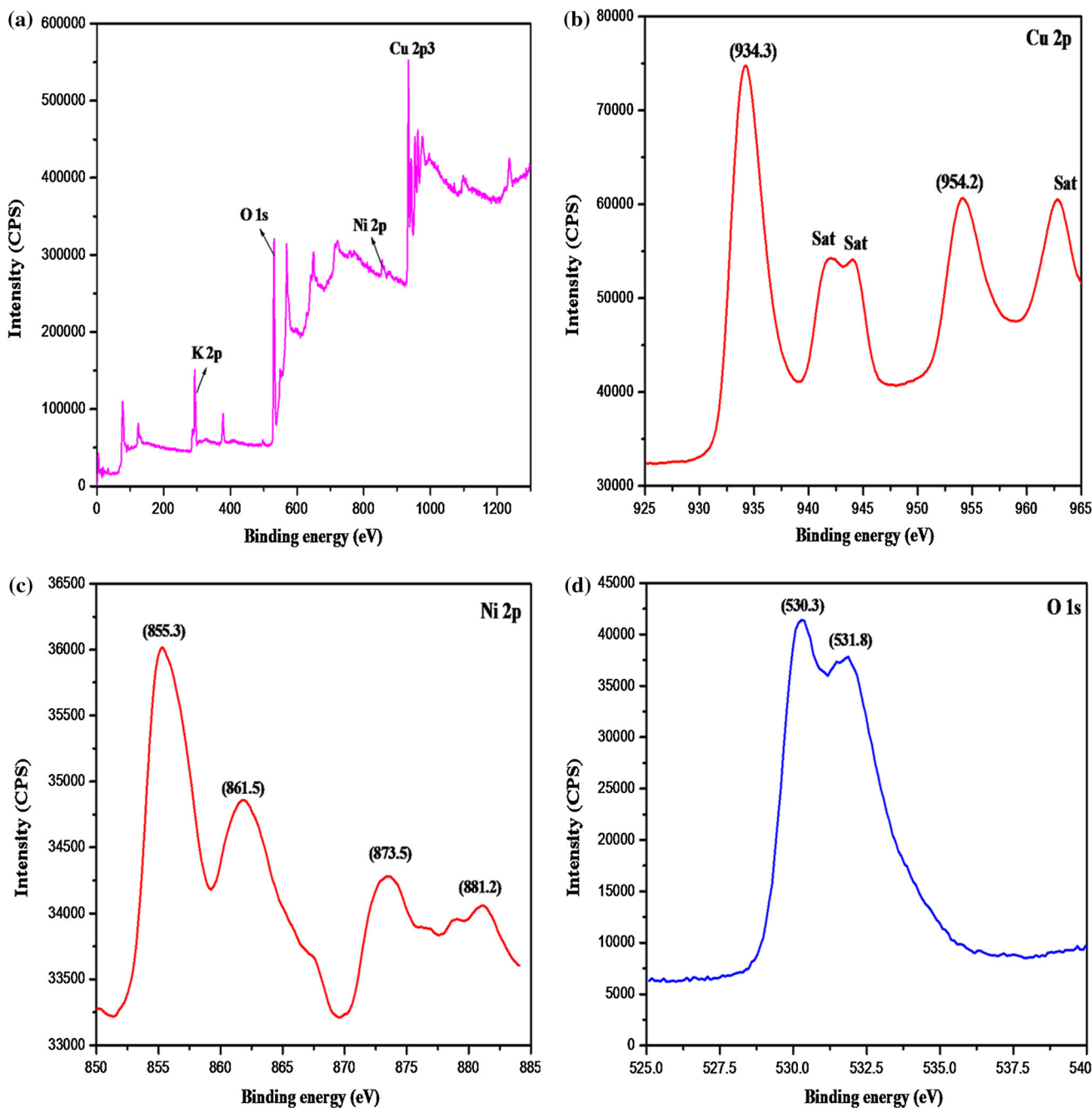| Samples	Particle size (nm)	Lattice parameters (Å)		
		a	b	c
CuO	21.41	4.058	3.423	5.062
CuO: Ni (0.05 M)	17.54	4.059	3.393	5.049
CuO: Ni (0.075 M)	15.35	4.052	3.425	5.048
CuO: Ni (0.1 M)	13.77	4.069	3.425	5.056
CuO: Ni (0.125 M)	25.43	4.063	3.422	5.0487

Fig. 2 XPS spectra of (0.1 M) Ni doped CuO nanoparticles. **a** surface scan, **b** Cu 2p, **c** Ni 2p and **d** O 1s

3.3 Optical properties

3.3.1 Ultra violet–visible–diffuse reflectance spectroscopy

The optical properties of pure and Ni doped CuO nanoparticles were analysed by UV–Vis–DRS spectra. The recorded DRS spectra are shown in Fig. 3a. For the purpose of obtaining band gap values of CuO and Ni incorporated CuO the well-known Eq. (2) was used.

$$\alpha = \frac{A \left(h\nu - E_g \right)^{1/2}}{h\nu} \tag{2}$$

Where α, E_g and A are the absorption coefficient, band gap, and constant, respectively. By extrapolating the linear region in the plots of $(\alpha h\nu)^{1/2}$ versus $h\nu$ (Fig. 3b), the calculated E_g values of pure and Ni-doped CuO nanoparticles with 0.05, 0.075, 0.1 and 0.125 M of Ni system are 1.95, 2.05, 2.11, 2.17 and 2.25 eV, respectively. The band
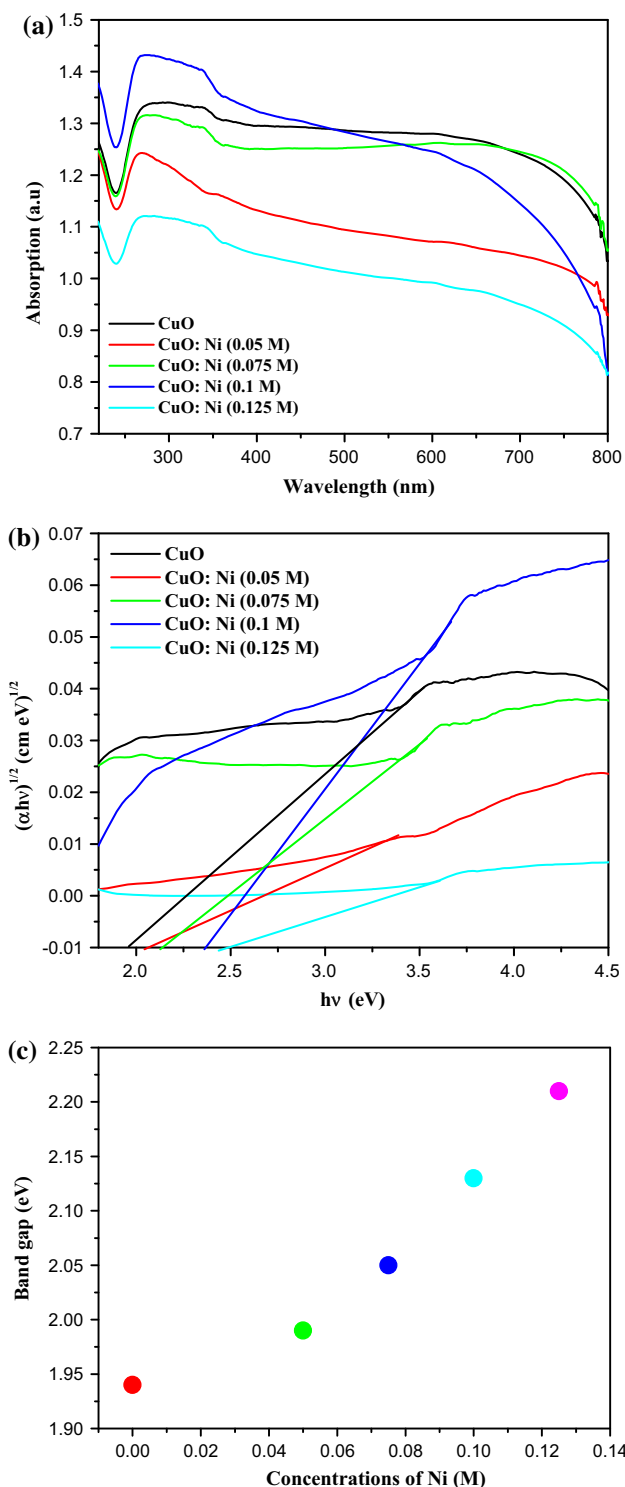
Fig. 3 **a** UV–Vis–DRS absorption spectra of CuO and various concentrations of Ni-doped CuO nanoparticles. **b** Plot of band gap energy for pure and Ni doped CuO nanoparticles. **c** Band gap values of the CuO nanoparticles as a function of Ni concentration

gap values versus nickel concentrations of the growth behavior are plotted in Fig. 3c. On increasing the concentration of Ni doping, the E_g values are increases with

increase in Ni content. Because, the E_g of the NiO ($E_g = 4$ eV) is higher than that of CuO ($E_g = 1.95$ eV for the present work). The band gap of Ni-doped CuO should be greater than that of pure CuO nanoparticles. When increasing Ni doping concentration, the peak intensity of all the doped samples increases compared to pure CuO nanoparticles.

3.3.2 Photoluminescence study

PL emission spectra of pure and Ni doped CuO nanoparticles were measured at room temperature with an excitation wavelength of 330 nm, as shown in Fig. 4. It exhibits the higher intensity of the green emission band at 527 nm in the visible region. Significantly, the green emission band for the powders are not due to the band gap emission, but can be attributed to various structural defects and singly ionized oxygen vacancy present in pure and Ni-doped CuO samples. When compared with CuO, the peaks of doped products are getting broadened with intensity enhancement. The potential reason for the intensity increase is increased recombination of electrons with the holes in the single ionized oxygen vacancy [23].

3.4 Functional group analysis

FT-IR spectroscopy is an important tool to study the presence of functional groups in the given sample. Figure 5 shows the FT-IR spectra of pure and different levels of Ni^{2+} doped CuO samples. All the samples show absorption bands at 1109 cm^{-1} may be attributed to –OH bending vibrations of Cu–OH [24]. The peaks around at 1020–588 cm^{-1} are associated to the metal–oxygen stretching of CuO. The absorption band observed at
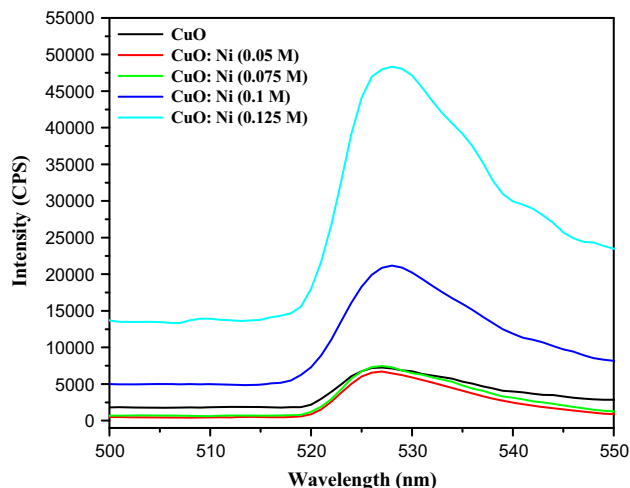

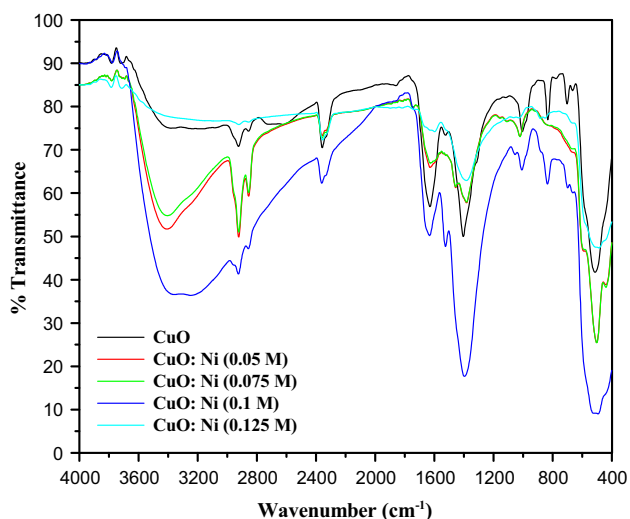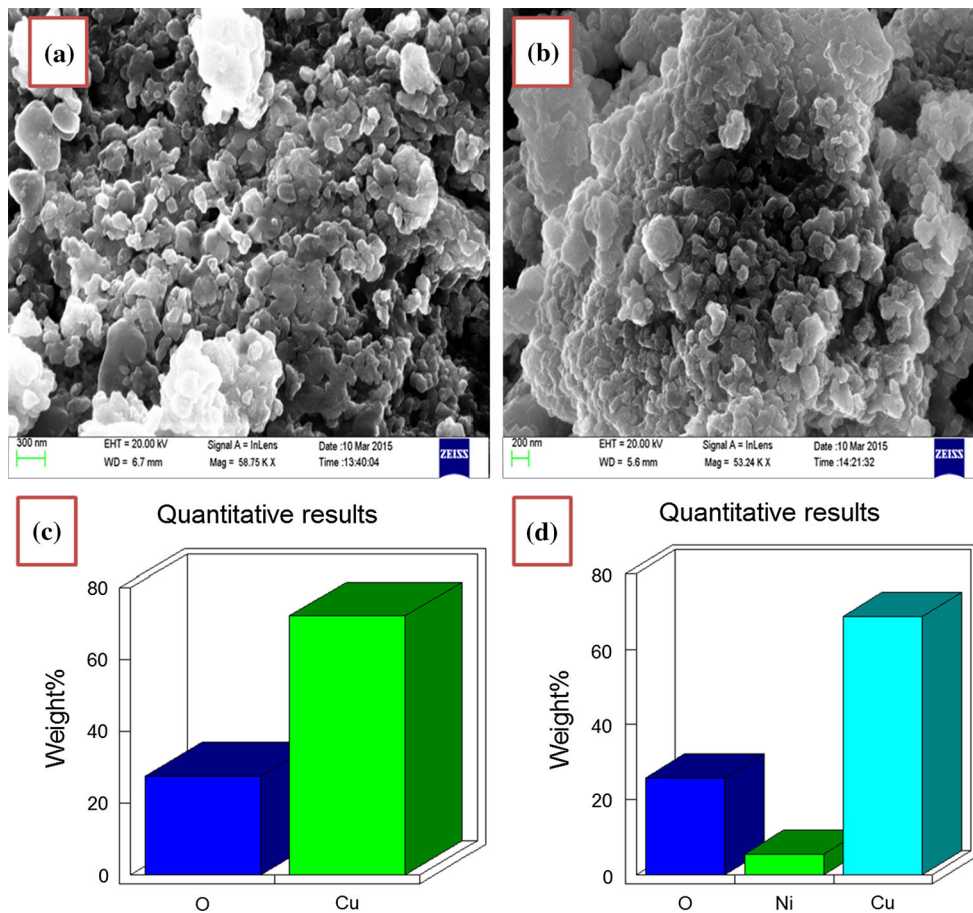**Fig. 4** PL emission spectra of CuO and various concentrations of Ni-doped CuO nanoparticles

Fig. 5 FTIR spectra of CuO and various concentrations of Ni-doped CuO nanoparticles

501 cm^{-1} corresponds to CuO with monoclinic structure [25]. The strong peaks obtained at 588 and 501 cm^{-1} are assigned to the characteristic stretching vibrations in monoclinic CuO. The appearance of higher frequency mode at 588 cm^{-1} is attributed to Cu–O stretching along

(101) direction and the mode at 501 cm^{-1} is due to Cu–O stretching along (101) [26]. The bands at 1644 and 3406 cm^{-1} could be assigned to the bending and stretching vibrations of –OH group respectively which may be present due to adsorbed water molecules. The peaks observed at 1382 and 1020 cm^{-1} are ascribed to the O–C=O symmetric and asymmetric stretching vibrations.

The addition of higher doping concentration of Ni (0.125 M), the FT-IR spectra of Ni doped CuO nanoparticles show strong band at 439 cm^{-1} corresponds to the vibration of Ni bond [27]. Some other weak bands are also appeared at 2922, 2856, 2358 and 1382 cm^{-1} probably due to the C–H stretching modes arising from the presence of surfactant molecules associated with the Cu Ni alloy nanoparticles [28].

3.5 Morphological analysis

3.5.1 FE-SEM

Figure 6a, b shows the FE-SEM images of pure and Ni doped CuO nanoparticles. From the photographs, it can be clearly observed that the nanoparticles exhibit flower-like morphology. The magnification of a flower like aggregate
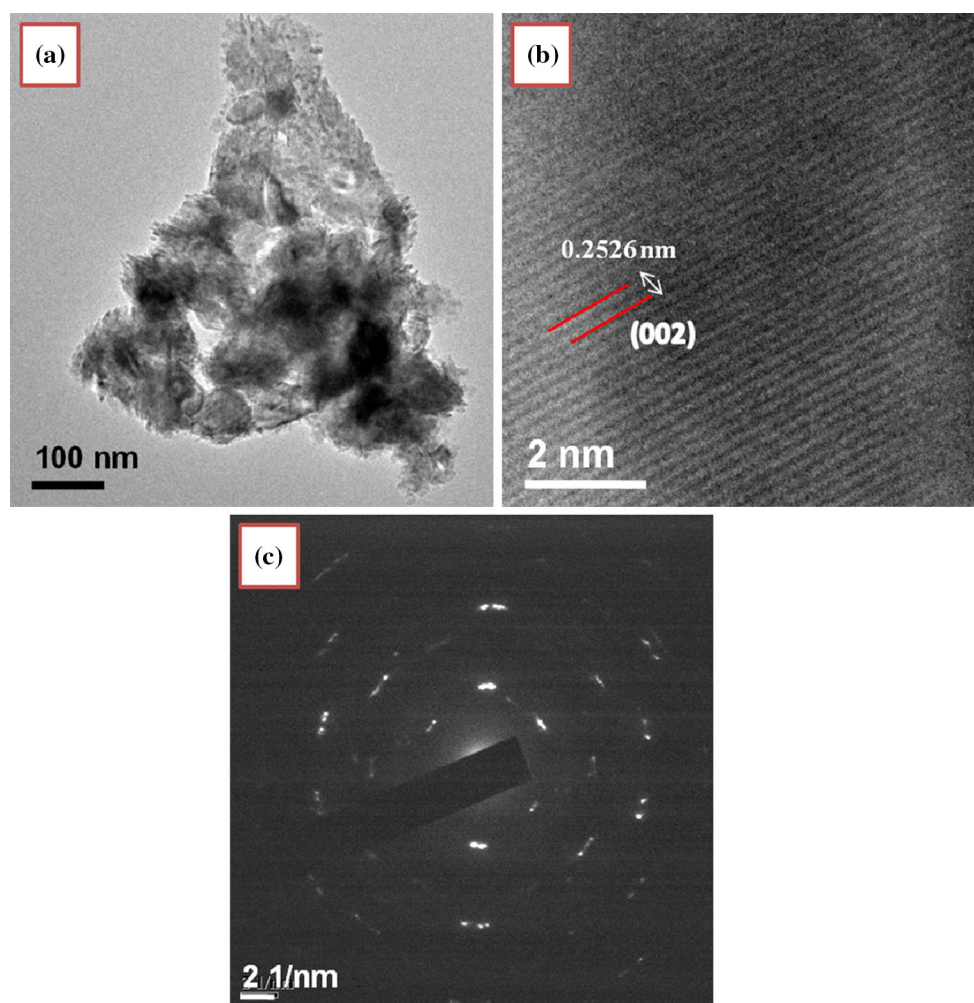
Fig. 6 a, b FE-SEM images of pure and (0.1 M) Ni doped CuO nanostructure and **c, d** corresponding quantitative results

Fig. 7 TEM image of CuO nanostructures (**a**), corresponding HR-TEM image (**b**) and SAED patterns (**c**)

from each nanoparticle is shown in Fig. 6b. It can be seen that the products are composed of a large amount of flowerlike aggregates and that most of them are uniform in shape. The rate of particle aggregation is a major factor that controls the morphology and structure (crystalline) of the final product. In Fig. 6c, d shows the quantitative results of pure and Ni doped CuO. The quantitative results show the presence of 70 wt% (57.91 at.%) Cu, 5 wt% (3.33 at.%) Ni and 25 wt% (38.76 at.%), oxygen and hence indicate the purity of CuO nanoparticles. It is also evident to notice that the prepared Ni-doped CuO compositions are pure and free of elemental impurities.

3.5.2 Transmission electron microscopy

The TEM image revealed that the growth has taken place by ''cluster by cluster'' of the nanocrystals. Thus, TEM image (Fig. 7a) shows that the particles exhibit CuO spongy like structure. These tiny nanocrystals grow together to form clusters of CuO flower. Figure 7c shows the characteristic rings in the selected area electron diffraction pattern (SAED). It is clear from SAED images; the circles contain bright spots which confirm the crystallinity of the synthesized nanoparticles. In Fig. 7b, the HR-TEM image shows that the continuous lattice fringes with the interplanar spacing of 0.2526 nm which is in good agreement with the interplanar distance of (002) plane of the monoclinic structure of CuO. Typical TEM images of Ni doped CuO nanoparticles are shown in Fig. 8a. It clearly shows uniform particles with a hexagonal shape. However, TEM image of Ni nanoparticles reveal a hexagonal morphology. Figure 8b also shows the inter-planar spacing (0.2524 nm) corresponding to the (002) plane. This confirms the results of XRD pattern.

3.6 Magnetic behaviour

Magnetic behavior of the synthesized Undoped and Ni doped CuO nanoparticles are studied at room temperature. The M–H curve shows the ferromagnetic nature and also
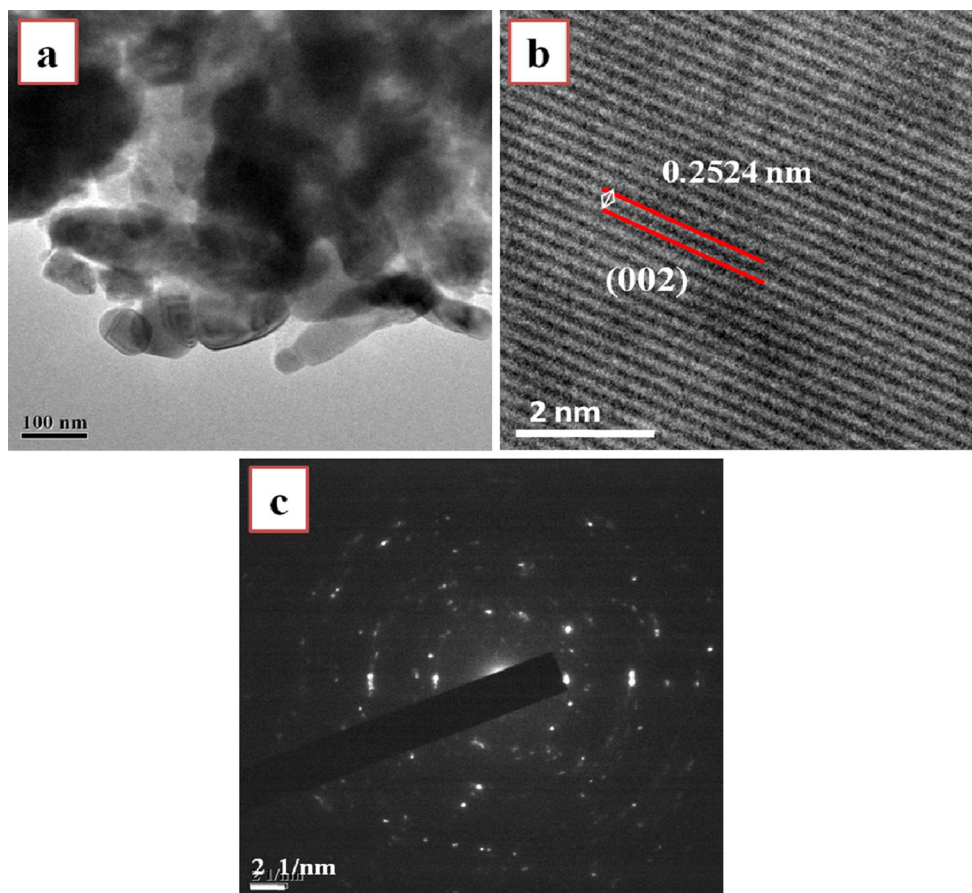
Fig. 8 TEM images of (0.1 M) of Ni doped CuO nanostructures (**a**), corresponding HR-TEM image (**b**) and SAED patterns (**c**)
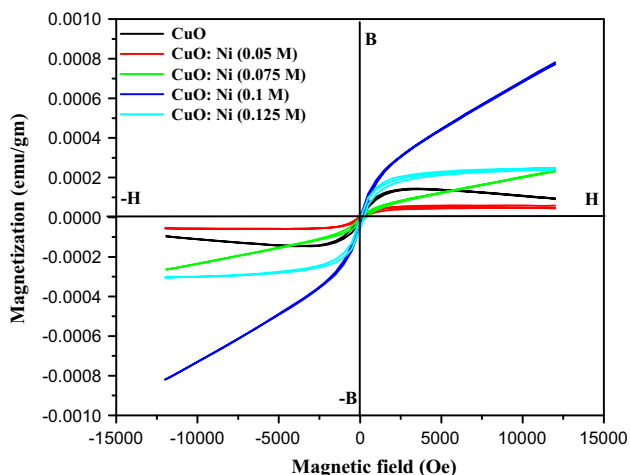

Fig. 9 Magnetization versus magnetic field (M–H) plots at room temperature of pure CuO and various levels Ni doped CuO nanoparticles

the change in behavior of hysteresis curve with respect to the doping concentration. Figure 9 represents VSM curve of Ni-doped CuO sketched at room temperature. Ni

doping shows variation in the trends of magnetic behavior and the 0.1 M Ni doped exhibits s narrow loop seems to be interesting outcome. Remarkable changes in the shape and width of hysteresis loop shows soft magnetic nature. The strong ferromagnetic moments in the doped samples may be due to the variation in the magnetic moments of Ni^{2+} ions substitution in Cu^{2+}. The magnetic moments of Cu^{2+}, Ni^{2+} are 1.73, and 2.83 μB, respectively, in high spin state. From the above statement the magnetic moments of Ni ions are larger than the Cu ions thus the doping induces stronger ferromagnetic behaviour. Similar results were reported by Meneses et al. [29] and Arbuzova et al. [30]. With the increase in Ni doping there is an appreciable variation in the saturation magnetization (M_S) and Coercitivity (H_C). M–H curve for 0.05 M of Ni shows a hysteresis loop with a minimum M_S value of 59.903×10^{-6} emu/g and H_C value of 158.68 (Gauss). For 0.1 M Ni content, M_S reaches a maximum value of 800.58×10^{-6} emu/g with lesser H_C value as given in Table 2.
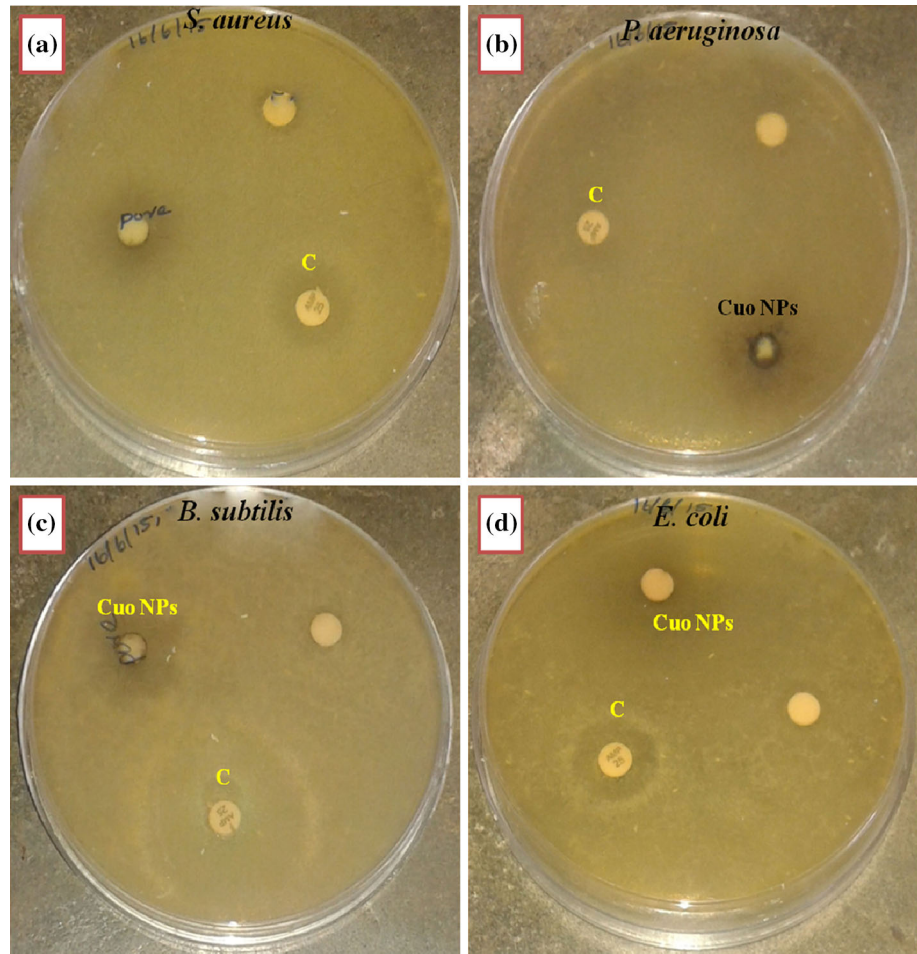
The enhancement of ferromagnetism in Ni-doped CuO samples may also be due to the formation of oxygen

Table 2 Magnetic behaviors of CuO and CuO: Ni^{2+} nanoparticles

Sample	Saturation magnetization (emu/gm) $\times 10^{-6}$	Coercivity (Gauss)
CuO	145.26	118.90
CuO: Ni^{2+} (0.05 M)	59.903	158.68
CuO: Ni^{2+} (0.075 M)	249.49	111.79
CuO: Ni^{2+} (0.1 M)	800.58	89.642
CuO: Ni^{2+} (0.125 M)	276.75	109.83

Fig. 10 Zone of inhibition of pure CuO nanoparticles. **a** *Staphylococcus aureus*, **b** *Pseudomonas aeruginosa*, **c** *Bacillus subtilis* and **d** *Escherichia coli*

vacancies. Thus doped Ni ion scan "trap" the free electrons emitted by the oxygen vacancies, which may result in the enhancement of the ferromagnetic spin–spin interaction between nickel and copper atoms.

3.7 Antibacterial activity

The synthesized Ni doped and pure CuO nanoparticles were subjected to study the antibacterial activity against two Gram positive (*Staphylococcus aureus* and *Bacillus subtilis*) and Gram negative (*Pseudomonas acruginosa* and *Escherichia coli*) pathogens by agar well diffusion method (Figs. 10 and 11). As indicated in the Table 3, all the samples show acceptable antibacterial activity. However, when compared to positive control, the antimicrobial response of CuO is enhanced only at higher levels of Ni-doping. Among the pathogens studied, *B. Subtilis* and *E. coli* show case higher antimicrobial activity as positive control does.

The possible mechanism involved in the antimicrobial activity can be ascribed from the disruption of cell membrane due to the release of copper ions from CuO nanoparticles, which attach to negatively charged bacterial cell wall and rupture it, thereby leading protein

Fig. 11 Zone of inhibition of
Ni doped CuO nanoparticles.
a *Staphylococcus aureus*,
b *Pseudomonas aeruginosa*,
c *Bacillus subtilis* and
d *Escherichia coli*
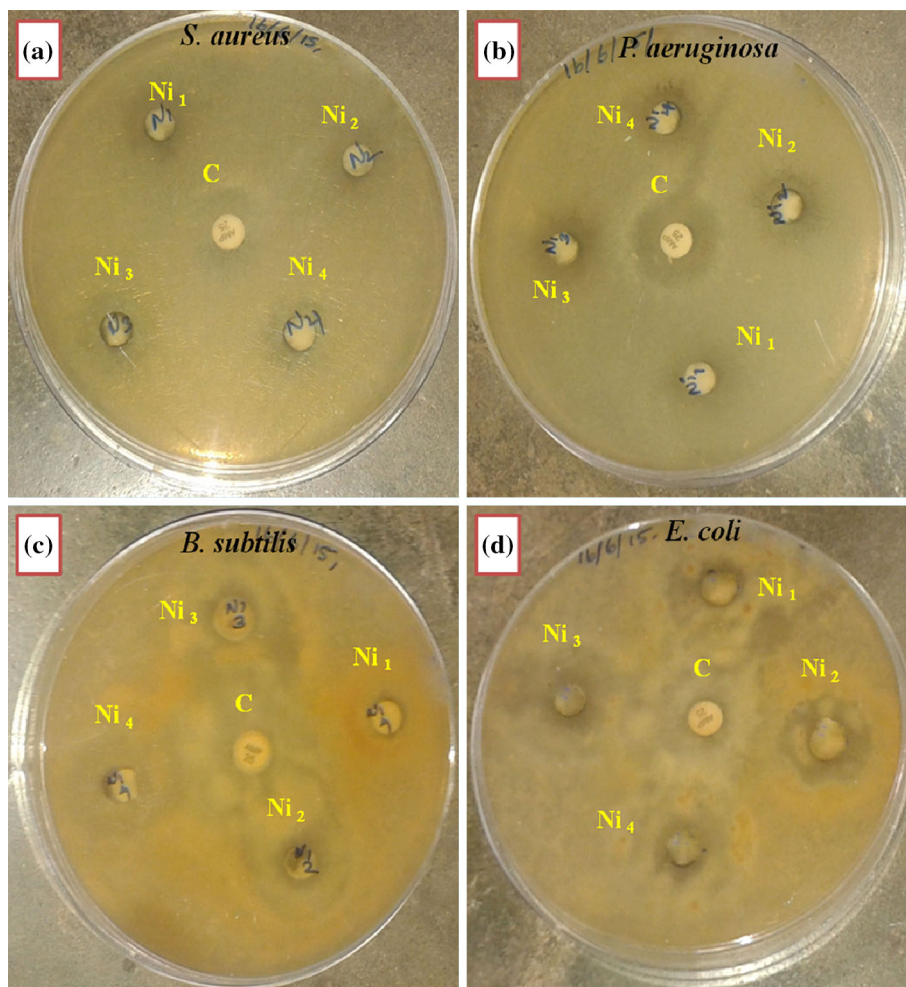
denaturation and cell death [31, 32]. After giving its entry into the bacterial cell, Cu may bind to deoxyribonucleic acid molecules and get involved in the cross-linking of nucleic acid strands, forming a disorganized helical structure. In addition, the intake of Cu can also tailor the biochemical processes of bacterial cells. As we increase the Ni^{2+} content, it replaces more and more Cu^{2+} and resulted in higher antimicrobial activity. The less permeable nature of *B. subtilis* and *E. coli* provides a state way for the entry of Cu^{2+} ions and leads to high rate of cell death.

4 Conclusions

Pure and Ni doped CuO nanoparticles have been successfully synthesized by chemical precipitation method. The XRD results reveal that Ni ions are well substituted in CuO lattice and NiO content presented in higher level doping

(0.125 M). This is also confirmed by FT-IR analysis. XPS study shows the bivalent state of Cu and Ni in the Ni–CuO matrix. From UV–Vis–DRS results, it could be found that the optical band gap was gradually increased with Ni doping concentration. The room temperature PL spectra reveal that the increase in the intensity of a green emission by increasing the concentration of nickel ion. The FE-SEM and TEM images show the morphological changes by the effect of doping element in CuO nanoclusters. The lattice fringes seen in HR-TEM are in good agreement with the interplanar distance of (002) plane. According to the magnetic measurements, Ni-doped CuO exhibits a ferromagnetic behaviour at room temperature, and is dependent on the amount of dopant (Ni^{2+}) ions. The origin of the observed room temperature ferromagnetism is most likely due to the intrinsic defects. The antibacterial behavior of the synthesized products of doped and undoped CuO exhibits the maximum zone of inhibition for *B. subtilis* and *E. coli*.

Table 3 Antibacterial activity of pure and Ni doped CuO nanoparticles against two gram-positive and gram-negative bacteria

Micro organisms	Samples	Zone of inhibition (mm)	
		Positive control	Negative control
P. aeruginosa	P	10	7
	Ni$_1$	18	7
	Ni$_2$	18	9
	Ni$_3$	18	11
	Ni$_4$	18	12
S. aureus	P	15	7
	Ni$_1$	15	10
	Ni$_2$	15	12
	Ni$_3$	15	14
	Ni$_4$	15	15
B. subtilis	P	15	10
	Ni$_1$	20	10
	Ni$_2$	20	17
	Ni$_3$	20	17
	Ni$_4$	20	19
E. coli	P	12	6
	Ni$_1$	20	12
	Ni$_2$	20	16
	Ni$_3$	20	17
	Ni$_4$	20	18

References

1. Y. Zhang, X. Bo, A. Nsabimana, H. Wang, M. Li, L. Guo, Analyst **138**, 3633 (2013)
2. N. Mohamed Basith, J. Judith Vijaya, L. John Kennedy, M. Bououdin, Mater. Sci. Semi. Process **17**, 110–118 (2014)
3. C.T. Meneses, J.G.S. Duque, L.G. Vivas, M. Knobel, J. Non-Cryst, Solids **354**, 4830–4832 (2008)
4. G.N. Rao, Y.D. Yao, W.J. Chen, J. Appl. Phys. **101**, 09–119 (2007)
5. Y. Gulen, F. Bayansal, B. Sahin, H.A. Cetinkara, H.S. Guder, Ceram. Int. **39**, 6475–6480 (2013)
6. H.D. Colorado, G.A. Perez Alcazar, Hyperfine Interact. **202**, 139–144 (2011)
7. S. Manna, S.K. De, J. Magn. Magn. Mater. **322**, 2749–2753 (2010)
8. K.L. Liu, S.L. Yuan, H.N. Duan, X.F. Zheng, S.Y. Yin, Z.M. Tian, C.H. Wang, S.X. Huo, J. Appl. Phys. **107**, 023911–023911-4 (2010)
9. D.T. Gazioglu, F. Dumludag, A. Altindal, AIP Conf. Proc. **1203**, 456–460 (2010)
10. M.R. Vaezi, M. Barzegar Vishlaghi, M. Farzalipour Tabriz, O. Mohammad Moradi, J. Alloys Compd. **635**, 118–123 (2015)
11. D. Li, Y.H. Leung, A.B. Djurisic, Z.T. Liu, M.H. Xie, J. Gao, W.K. Chan, J. Cryst. Grow. **282**, 105–111 (2005)
12. Y. Dang Hai, L. Zhang Yu, K. Liang Jing, S. Xie Si, J. Mater. Sci. **28**, 5176–5178 (1993)
13. C. Yang, X.T. Su, J.D. Wang, X.D. Cao, S.J. Wang, L. Zhang, Sens. Actuators B Chem. **185**, 159–165 (2013)
14. B. Toboonsung, P. Singjai, J. Alloys Compd. **509**, 4132–4237 (2011)
15. Y. Li, M. Xu, L. Pan, Y. Zhang, Z. Guo, B. Chong, C. Bi, J.Q. Xiao, J. Appl. Phys. **107**, 113908–113908-6 (2010)
16. S. Anandan, G.J. Lee, J.J. Wu, Ultrason. Sonochem. **19**, 682–686 (2012)
17. H. Raja Naika, K. Lingaraju, K. Manjunath, D. Kumar, G. Nagaraju, D. Suresh, H. Nagabhushana, J. Tai. Univ. Sci. **19**(1), 7–12 (2014)
18. N. Kannadasan, N. Shanmugam, S. Cholan, K. Sathishkumar, G. Viruthagiri, R. Poonguzhali, Mater. Charact. **97**, 37–46 (2014)
19. M. Huang, Y. Zhang, F. Li, Z. Wang, Alamusi, N. Hu, Z. Wen, Q. Liu, Sci. Rep. **4**, 4518 (2014)
20. C. Zhou, L. Xu, J. Song, R. Xing, S. Xu, D. Liu, H. Song, Sci. Rep. **4**, 7382 (2014)
21. M. Yin et al., J. Am. Chem. Soc. **127**, 9506–9511 (2005)
22. M. Ashokkumar, S. Muthukumaran, J. Lumin. **162**, 97–103 (2015)
23. Z. Hussain Ibupoto, K. Khun, V. Beni, X. Liu, M. Willander, Sensors **13**, 7926–7938 (2013)
24. Z. Yang, C.K. Chiang, H.T. Chang, Nanotechnology **19**, 25604–25608 (2008)
25. M. Abdelaziz, E.M. Abdelrazek, Phys. B **390**, 1–9 (2007)
26. B. Balamurunga, B.R. Mehta, Thin Solid Films **396**, 90–96 (2001)
27. Y. Xu, D. Chen, X. Jiao, J. Phys. Chem. B **109**, 13561–13566 (2005)
28. K.M. Mayya, N. Jain, A. Gole, D. Langevin, M. Sastry, J. Colloid Interf. Sci. **270**, 133–139 (2004)
29. R.A. Mac Phail, H.L. Strauss, R.G. Snyder, J. Phys. Chem. **88**, 334–341 (1984)
30. C.T. Meneses, J.G.S. Duque, L.G. Vivas, M. Knobel, J. Non-Cryst. Solid. **354**, 4830–4832 (2008)
31. I. Sondi, B.S. Sondi, J. Colloid Interf. Sci. **275**, 177–182 (2004)
32. A. Azam, A.S. Ahmed, M. Oves, M.S. Khan, A. Memic, Int. J. Nanomed. **7**, 3527–3535 (2012)